Research Article Vol. 30, No. 9 / 25 Apr 2022 / Optics Express 15310
Optics EXPRESS

Transverse light-shift in a spin-exchange relaxation-free co-magnetometer: measurement, decoupling, and suppression

SIXUN LIU,[1,2] RUIGANG WANG,[1,2] LINLIN YUAN,[1,2] JIAQI WU,[1,2] QI YUAN,[1,2] JUN ZHU,[1,2] WENFENG FAN,[1,3,4] ZHUO WANG,[1,3,5] AND PENGCHENG DU[1,3]

[1] *Beihang Hangzhou Innovation Institute Yuhang, Beihang University, Hangzhou 310023, China*
[2] *School of Instrumentation and Optoelectronic Engineering, Beihang University, Beijing 100191, China*
[3] *The Research Institute for Frontier Science, and The Key Laboratory of Ministry of Industry and Information Technology on Quantum Sensing Technology, Beihang University, Beijing 100191, China*
[4] *fanwenfeng@buaa.edu.cn*
[5] *zhuowang@buaa.edu.cn*

Abstract: The transverse light-shift can induce non-negligible polarization error in the output signal of spin-exchange relaxation-free (SERF) co-magnetometer. In this paper, a novel method for rapid measurement of transverse light-shift based on the error of steady-state response of co-magnetometer is proposed firstly, then the sources of transverse light-shift in a compact SERF co-magnetometer is modeled and analyzed from three aspects: the non-ideal linear polarization of probe laser, the circular dichroism of the atomic spin ensembles, and the stress-induced birefringence effect of the cell wall. Furthermore, the decoupling and suppression methods of transverse light-shift based on a degree of circular polarization (DOCP) regulation scheme is presented, to realize the decoupling measurement of the transverse light-shift introduced by the whole co-magnetometer cell, and cancel it out with the non-ideal linear polarization of the probe laser. Eventually, the DOCP regulation scheme suggested in this paper achieves more than a 67% suppression ratio in transverse light-shift, and the short- and long-term performance of SERF co-magnetometer are improved due to the reduction of the coupling effect between the probe laser power and transverse field. Moreover, the measurement, decoupling and suppression methods provided in this paper also have the potential to be applied to other atomic sensors, such as the SERF magnetometers and nuclear spin co-magnetometers.

1. Introduction

The SERF co-magnetometer contains two overlapping spin ensembles of alkali metal and noble gas inner a glass vapor cell [1]. With the effects of a resonant pump laser and high temperature, the electrons of alkali metal can be polarized and reach the SERF regime in an extremely weak magnetic field [2], in which the relaxation times and coherence are enhanced significantly [3,4]. Compared with nuclear magnetic resonance gyroscope, SERF co-magnetometer can achieve a higher sensitivity since the magnetic resonance linewidth cannot be broadened by the spin-exchange collisions. In addition, the magnetization produced by nuclear spin can follow and suppress the low frequency fluctuation on the transverse magnetic field such that SERF co-magnetometer has a self-compensation characteristic. Thus SERF co-magnetometer can be applied to inertial navigation as a high-precision rotation rate sensor [5–7]. Moreover, the SERF co-magnetometer has the potential to explore the frontiers of physics, like CPT and Lorentz violation [8–10], and search for spin-dependent forces [11–14].

The light-shift is produced when an off-resonant and circularly-polarized laser interacts with alkali metal atoms [15–17]. Since the light-shift cannot be consistently compensated by the coils

#456937 https://doi.org/10.1364/OE.456937
Journal © 2022 Received 23 Feb 2022; revised 3 Apr 2022; accepted 4 Apr 2022; published 20 Apr 2022

as the residual field inner the shield barrel, the coupled spin ensembles with high sensitivity of magnetic field deviate from the ideal compensation point such that the response and performance are degraded [18–21]. In engineering, enabling an open-loop compensation of the magnetic field for light-shift can suppress the cross-talk effect introduced by light-shift in the dual-axis SERF co-magnetometers [22,23], and the optimization for density ratio of different alkali metal atoms can mix and zero the total light-shift of them in the hybrid pumping SERF co-magnetometers [24,25]. The other methods for suppression or elimination of the light-shift, for example the magic wavelength in atomic clock [26,27], are always not applicable for the atoms in SERF regime.

Along with the further improvement of accuracy and stability in SERF co-magnetometer, the negative effects of the previously neglected transverse light-shift along the probe beam begin to be revealed and start to be studied in recent years [20,28,29], and the best reported bias instability of 0.00846 deg/h has been achieved by the probe laser intensity working point optimization [30]. The accurate measurement of the transverse light-shift is the basis for its study. However, the transverse light-shift is not as easy to measure as the longitudinal one along the pump beam due to its lower magnitude [3]. When the pump beam is not activated, the zero filed response of the co-magnetometer to the probe light can be applied to estimate its pumping effects offline [2], but that response cannot reflect the real transverse light-shift in practice engineering as the introduction of strong coupling between the electrons and nuclear spins. Recently, researchers proposed a novel measurement method based on the correlation between self-compensation point and laser power [29], while it is time-consuming for stabilization of the apparatus and the accuracy cannot be guaranteed due to the excessive amount of fitting involved in the calculation. Therefore, there is an urgent need to develop and improve the rapidity and accuracy of the method for acquiring transverse light-shift.

Theoretically, the light-shift is mainly affected by the following three natures of laser: degree of circular polarization (DOCP), optical power, and frequency [31]. Thus, it is intuitive to consider the optimization of these three factors above to reduce the transverse light-shift. Actually, the relation between the transverse light-shift and laser frequency satisfies a dispersion curve [24,32], and the sole zero crossing point is at the resonant frequency of transition, which cannot be employed to the optical rotation angle detection, such that the transverse light-shift cannot be eliminated by a laser frequency optimization scheme in principle. Since the laser power is proportional to the light-shift, the small laser spot or low laser power scheme can reduce the transverse light-shift [30,33], but also limit the signal-to-noise ratio and sensitivity of SERF co-magnetometer. Eventually, in this paper, a DOCP regulation scheme is proposed for suppression the transverse light-shift. Furthermore, except to the non-ideal linearly polarization of probe laser [2,3,16,29], there is absence of the studies on other sources of DOCP, especially on the polarization error induced by the optical characteristics of co-magnetometer cell.

The structure of this paper is as follows. Section 2 proposes a novel measurement method for the transverse light-shift firstly, then models and analyzes the sources of transverse light-shift from three aspects: the probe laser, the circular dichroism of the atomic spin ensembles, and the stress-induced birefringence effect of the cell wall, according to which the decoupling and suppression methods for the total transverse light-shift based on the DOCP regulation scheme are further developed. Section 3 describes the experimental setup of SERF co-magnetometer and its key components. Section 4 and 5 demonstrate the experimental verification and related conclusions for the measurement principles as well as decoupling and suppression methods in Section 2, respectively.

2. Theoretical analysis of the transverse light-shift

2.1. Measurement method

The dynamic behaviors of the polarization of atomic spin ensembles in SERF co-magnetometer cell containing alkali metal and noble gas can be well described by the coupled Bloch equations [34,35].

$$\begin{aligned} \frac{\partial \vec{P}^e}{\partial t} &= \frac{\gamma_e}{Q}\left(\vec{B}^n + \vec{B}^a + \vec{L}\right) \times \vec{P}^e - \vec{\Omega} \times \vec{P}^e + \frac{R_p \vec{s}_p + R_m \vec{s}_m + R_{se}^{en} \vec{P}^n - R_{tot}^e \vec{P}^e}{Q} \\ \frac{\partial \vec{P}^n}{\partial t} &= \gamma_n \left(\vec{B}^e + \vec{B}^a\right) \times \vec{P}^n - \vec{\Omega} \times \vec{P}^n + R_{se}^{ne} \vec{P}^e - R_{tot}^n \vec{P}^n \end{aligned} \tag{1}$$

where $\vec{P}^e$ and $\vec{P}^n$ are the electron and nuclear polarization. γ_e and γ_n are the electron and nuclear gyromagnetic ratio, $\vec{B}^a$ is the ambient magnetic field, $\vec{B}^e$ and $\vec{B}^n$ are magnetic fields generated by the magnetization of electron and nuclear spins, respectively. $\vec{\Omega}$ is the input rotation rate vector. Q is the slowing-down factor. R_p and R_m are the pumping rate from pump and probe beams, whose directions and DOCP are given by $\vec{s}_p$ and $\vec{s}_m$. R_{se}^{ne} and R_{se}^{en} are the spin-exchange rate induced by electrons and nuclei. R_{tot}^e and R_{tot}^n are the total relaxation rate of electron and nuclear spins, respectively. $\vec{L}$ is the light-shift composed of longitudinal and transverse components, where the longitudinal direction is defined as the propagation direction of the pump laser (z-axis), and the transverse direction is commonly defined as the propagation direction of probe laser (x- and y-axis). In this paper, the transverse light-shift only denotes the L_x since the absence of the y-axis probe beam in a single-axis co-magnetometer.

The off-resonant and circularly-polarized laser interacts with atoms can induce light-shift, which can be regarded as a fictitious dc magnetic field experienced by atoms. Theoretically, due to the presence of a polarization beam splitter (PBS) in front of the cell, the linearly polarized laser can not produce the transverse light-shift. However, as the extinction ratio of the actual PBS can not be infinite, the incident probe laser always contains the circularly polarized laser power component that can not be completely eliminated, which is also the focus of the recent literature [28,29]. Considering the energy level splitting effect of the probe laser near the wavelength to the resonance of the D1 transition in Rb, the transverse light-shift can be expressed as follows [3].

$$L_x = \frac{\Phi r_e c f}{A \gamma_e} \frac{\nu - \nu_0}{(\nu - \nu_0)^2 + (\Gamma/2)^2} \cdot s_l \tag{2}$$

where Φ is the photo flux proportional to the probe laser power I_0, i.e., $\Phi = I_0/\hbar\nu$, and $\hbar\nu$ represents the energy of a single photon. f is the oscillator strength of the D1 transition, A is the cross sectional area of the incident laser, ν is the probe laser frequency, Γ and ν_0 are the full-width at half maximum and the central frequency of the D1 transition , respectively. s_l is the DOCP of the incident probe laser and defined as the normalized difference in power for left-/right-handed circularly polarized laser [16].

$$s_l = \frac{I_{\sigma_+} - I_{\sigma_-}}{I_{\sigma_+} + I_{\sigma_-}} \tag{3}$$

According to a series of theories around the self-compensation point regime [2,3,25], the coil around the co-magnetometer cell produces a longitudinal compensation field $B^c = -B_z^e - B_z^n$, and also applies the transverse fields to zero the ambient fields composed of the residual fields generated by the magnetic shield $\delta B_{x/y}$ and the transverse light-shift L_x along the probe beam

Optics EXPRESS

direction.

$$\begin{aligned} B_x &= B_x^c + \delta B_x + L_x \\ B_y &= B_y^c + \delta B_y \end{aligned} \tag{4}$$

Furthermore, When considering to zero the magnetic field B_x along the x-axis, the $B_x B_z$ dependence relation is derived from the steady-state solution of Eq. (1).

$$P_x^e(B_x B_z) = \frac{\gamma_e P_z^e R_{\text{tot}}^e}{\left(R_{\text{tot}}^e\right)^2 + (\gamma_e)^2 (L_z + B_z)^2} \cdot \frac{B_x}{B^c} \cdot \left[\frac{\gamma_e (L_z + B_z)}{R_{\text{tot}}^e} B_z + \frac{P_z^n R_{se}^{en}}{P_z^e \gamma_e}\right] \tag{5}$$

Considering to employ an asymmetric modulation with peak-peak amplitude of ΔB_z when the deviation from the compensation point B_z is already close to zero, the corresponding transverse polarization satisfies that

$$\Delta P_x^e(B_x) = \frac{B_x}{B^c} \cdot \frac{(\gamma_e)^2 P_z^e (L_z + \Delta B_z) \Delta B_z}{\left(R_{\text{tot}}^e\right)^2 + (\gamma_e)^2 (L_z + \Delta B_z)^2} \propto B_x. \tag{6}$$

The co-magnetometer output signal S is determined by product of the transmission power I and optical rotation angle θ as below, whereas the magnitude of coefficient $\kappa(\nu, N)$ is only affected by probe laser frequency ν and alkali metal density N.

$$\begin{aligned} S =& 2I\theta \\ =& 2 \cdot I_0 \exp\left[-Ncr_e fl \frac{\gamma/2}{(\nu - \nu_0)^2 + (\gamma/2)^2}\right] \cdot \left[-\frac{1}{2} Nlr_e cf P_x^e \frac{\nu - \nu_0}{(\nu - \nu_0)^2 + (\gamma/2)^2}\right] \\ =& \kappa(\nu, N) I_0 P_x^e \end{aligned} \tag{7}$$

Substituting Eq. (2), Eq. (4) and Eq. (6) into the output signal expression Eq. (7), the error of steady-state response (ESSR) ΔS can be obtained:

$$\begin{aligned} \Delta S =& \kappa(\nu, N) I_0 \Delta P_x^e(B_x) \\ =& \kappa(\nu, N) I_0 B_x \frac{(\gamma_e)^2 P_z^e (L_z + \Delta B_z) \Delta B_z / B_c}{\left(R_{\text{tot}}^e\right)^2 + (\gamma_e)^2 (L_z + \Delta B_z)^2} \\ =& \kappa(\nu, N) \mathcal{F}(\Delta B_z) I_0 \left(B_x^c + \delta B_x + L_x\right) \\ =& \kappa(\nu, N) \mathcal{F}(\Delta B_z) \left[\mathcal{G}(\nu, \Gamma, A) I_0^2 + \left(B_x^c + \delta B_x\right) I_0\right] \end{aligned} \tag{8}$$

where the expressions of functions $\mathcal{F}$ and $\mathcal{G}$ are as below.

$$\begin{aligned} \mathcal{F}(\Delta B_z) &= \frac{(\gamma_e)^2 P_z^e (L_z + \Delta B_z)}{\left(R_{\text{tot}}^e\right)^2 + (\gamma_e)^2 (L_z + \Delta B_z)^2} \cdot \frac{\Delta B_z}{B^c} \\ \mathcal{G}(\nu, \Gamma, A) &= \frac{r_e cf}{\hbar \nu A \gamma_e} \cdot \frac{\nu - \nu_0}{(\nu - \nu_0)^2 + (\Gamma/2)^2} \cdot s_l \end{aligned} \tag{9}$$

From Eq. (8), ESSR can directly reflect the magnitude and sign of B_x. Ideally, if there is the absence of the transverse light-shift term in B_x, a constant field B_x^c produced by the coil can achieve the compensation for the residual magnetic field δB_x along the x-axis, and the relation of I_0-ΔS can be converted into a linear equation from a quadratic function. In that case, the probe laser power I_0 will have no effect on ESSR ΔS when B_x is completely compensated to zero.

Therefore, even though the transverse field has been compensated perfectly already, ESSR will still vary once the fluctuation of laser power occur due to the existence of the transverse light-shift. For illustrating this phenomenon, a reasonable response profile of SERF co-magnetometer is

Optics EXPRESS

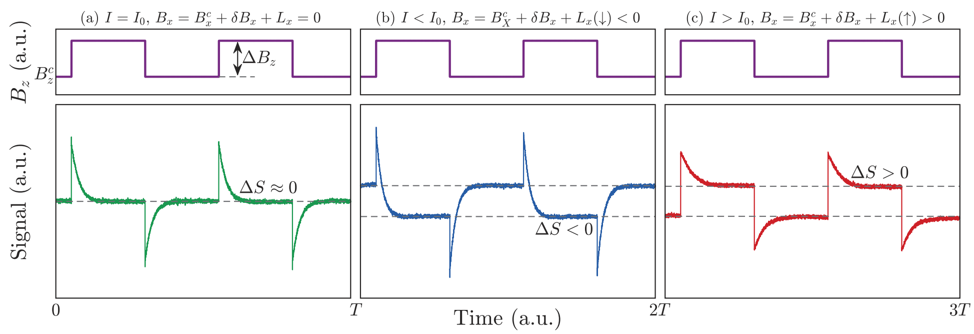

Fig. 1. The response profile under an applied asymmetric modulation field with peak-peak amplitude of ΔB_z: (a) $I = I_0$, and the ambient field B_x has been compensated perfectly by coil already. (b) The magnitude of transverse light-shift L_x decreases since the probe laser switches to a lower power level $I<I_0$ and (c) increases when it switches to a higher one $I>I_0$. Though both two cases (b) and (c) can result in $B_x \neq 0$, they still can be identified by ESSR ΔS.

plotted in Fig. (1). In additional, the polynomial coefficients of quadratic function (8) do not explicitly contain the transverse light-shift $L_x = \mathcal{G}I_0$, which means that one cannot obtain the exact information of L_x by a simple polynomial fitting on the I_0-ΔS curve.

Thereby we come up with an ingenious measurement method: first calibrate ESSR versus the ambient magnetic field B_x near the transverse compensation point of SERF co-magnetometer under M different probe laser powers I_k $(k = 1, 2, \ldots, M)$.

$$C_k = \frac{\partial \Delta S}{\partial B_x} = \kappa(\nu, N)\mathcal{F}(\Delta B_z) I_k \quad (k = 1, 2, \ldots, M) \tag{10}$$

Based on the calibration results C_k, one can measure the ESSR ΔS_1 at the compensation point B_{x1}^c of SERF co-magnetometer corresponding to the first laser power point I_1, then fix the compensation point at B_{x1}^c and rapidly switch to the M-th laser power point in sequence to acquire their corresponding ΔS_k, and the ratio $\mathcal{R}_k = \Delta S_k / C_k$ denotes the deviation of the ambient magnetic field B_{xk} of SERF co-magnetometer from the zero field under the k-th laser power point.

$$\mathcal{R}_k = \frac{\Delta S_k}{C_k} = B_{x1}^c + \delta B_x + L_{xk} = B_{x1}^c + \delta B_x + \mathcal{G} I_k \quad (k = 1, 2, \ldots, M) \tag{11}$$

From Eq. (11), the transverse light-shift varies synchronously with the switching of the optical power and results in a direct departure of the ambient magnetic field from the zero field, hence the relative variation in transverse light-shift δL_x is implied in this deviation and can be defined as Eq. (12). Furthermore, it is noteworthy that a perfect zero of the ambient magnetic field cannot be implemented due to the finite compensation precision of the actual coil, i.e., $\mathcal{R}_1 \neq 0$, thus we choose to exploit the relative variation δR_k to represent the δL_{xk} instead of $\mathcal{R}_k$.

$$\delta L_{xk} \triangleq \delta \mathcal{R}_k = \mathcal{R}_k - \mathcal{R}_1 = L_{xk} - L_{x1} = \mathcal{G}(I_k - I_1) \quad (k = 1, 2, \ldots, M) \tag{12}$$

According to Eq. (12), it is clear that the relation of the relative variation of transverse light-shift versus the probe laser power, i.e., the I-δR curve, is theoretically linear. Moreover, the intercept value $-\mathcal{G}I_1$ of the I-δR curve can be inverted to obtain the transverse light-shift L_{x1} corresponding to the first probe laser power I_1.

Ultimately, the transverse light-shift of SERF co-magnetometer under k-th probe laser power I_k can be obtained as follows, the experimental procedure and measurement results based on the above measurement method are stated in detail in Section 4.

$$L_{xk} = \delta R_k + \mathcal{G} I_1 \quad (k = 1, 2, \ldots, M) \tag{13}$$

Optics EXPRESS

2.2. Decoupling and suppression methods

The co-magnetometer based on SERF regime is sensitive to weak fluctuations of the ambient magnetic field [18,36], yet the presence of transverse light-shift causes the coupling between the probe laser power and the transverse magnetic field, which means that fluctuations in the laser power unexpectedly introduce instability in the transverse magnetic field, thus making the long-term stability of SERF co-magnetometer further degraded. More than that, L_x also results in variation in the transverse polarization P_x^e, which reduces the sensitivity of SERF co-magnetometer to the magnetic field.

Therefore, besides proposing the measurement method of transverse light-shift, we proceed to develop the decoupling and suppression methods against the transverse light-shift based on a DOCP regulation scheme.

According to the numerator of Eq. (2), the achievement of the elimination of transverse light-shift must satisfies $\Phi(\nu-\nu_0)s_l=0$. Considering that neither $\Phi=0$ nor $\nu=\nu_0$ can realize the detection of optical rotation, $s_l=0$ seems to be the only approach to completely eliminate L_x. However, due to the circular dichroism of the polarized atomic spin ensembles [2,3], whose different absorption for the left-/right-handed circularly polarized components will also result in elliptical polarization of the probe beam as it propagates within the cell. By the selection rule [37], the populations $\rho_\pm$ of the ground states $m_s=\pm 1/2$ only interact with $\sigma_\mp$ laser components, and the imaginary part of the refractive index $n_\mp$ of the atomic spin ensembles from the macroscopic point of view is shown below.

$$\mathrm{Im}\left[n_\pm(\nu)\right]=\rho_\mp\frac{c^2Nr_ef}{2\pi\nu}\cdot\frac{\Gamma/2}{(\nu-\nu_0)^2+(\Gamma/2)^2} \tag{14}$$

When a linearly polarized laser with the power I_0 is incident into the co-magnetometer cell with the diameter $\mathcal{L}$, and its vibration direction is horizontal, the incident laser can be described by Jones vector $\vec{E}(0)$ and further decomposed into two components of equal power along an orthonormal basis $(\vec{E}_{\sigma_+},\vec{E}_{\sigma_-})$ as follows.

$$\begin{gathered}\vec{E}(0)=\sqrt{I_0}\begin{pmatrix}1\\0\end{pmatrix}=\sqrt{\frac{I_0}{2}}\left[\vec{E}_{\sigma_+}+\vec{E}_{\sigma_-}\right]=\sqrt{\frac{I_0}{2}}\begin{pmatrix}1/\sqrt{2}\\ i/\sqrt{2}\end{pmatrix}_{\sigma_+}+\sqrt{\frac{I_0}{2}}\begin{pmatrix}1/\sqrt{2}\\ -i/\sqrt{2}\end{pmatrix}_{\sigma_-}\\ I_{\sigma_+}(0)=I_{\sigma_-}(0)=\frac{I_0}{2}\end{gathered} \tag{15}$$

While the laser is incident to the position within the cell at a depth of l, a simplified Beer's law is considered to describe the light absorption rather than the complete Beer-Lambert law due to the slight DOCP of probe beam.

$$I_{\sigma_\pm}(l)=I_{\sigma_\pm}(0)\exp\left(-\frac{2\nu l\,\mathrm{Im}\left[n_\pm(\nu)\right]}{c}\right) \tag{16}$$

In this case, the circular dichroism expressed in Eq. (16) leads to a phase retardation δ in the vertical component of the beam with respect to the horizontal direction, which indicates the inevitable introduction of elliptical polarization of the probe beam by the circular dichroism of atomic spin ensembles.

$$\begin{aligned}\vec{E}(l) &= \sqrt{I_{\sigma_+}(l)}\begin{pmatrix}1/\sqrt{2}\\ i/\sqrt{2}\end{pmatrix}_{\sigma_+} + \sqrt{I_{\sigma_-}(l)}\begin{pmatrix}1/\sqrt{2}\\ -i/\sqrt{2}\end{pmatrix}_{\sigma_-}\\ &= \frac{\sqrt{2}}{2}\begin{pmatrix}\sqrt{I_{\sigma_+}(l)}+\sqrt{I_{\sigma_-}(l)}\\ i\left[\sqrt{I_{\sigma_+}(l)}-\sqrt{I_{\sigma_-}(l)}\right]\end{pmatrix}\\ &= \frac{\sqrt{I_{\sigma_+}(l)}+\sqrt{I_{\sigma_-}(l)}}{\sqrt{2}}\begin{pmatrix}1\\ i\delta(l)\end{pmatrix}\end{aligned} \tag{17}$$

where the phase retardation $\delta(l) = \frac{\sqrt{I_{\sigma_+}(l)}-\sqrt{I_{\sigma_-}(l)}}{\sqrt{I_{\sigma_+}(l)}+\sqrt{I_{\sigma_-}(l)}}$, and the DOCP of probe laser induced by the circular dichroism of atomic spin ensembles can be expressed in terms of δ as below.

$$s_a(l) = \frac{2\delta(l)}{1+\delta^2(l)} \tag{18}$$

The DOCP introduced by circular dichroism diminishes with the detuning of the probe laser, as shown in Fig. 2(a), but the magnitude of the pressure in the cell is proportional to the broadening of the linewidth, which makes the DOCP at the far detuning still non-negligible. Not only that, the length of the optical path through the cell also affects the DOCP, as shown in Fig. 2(b).

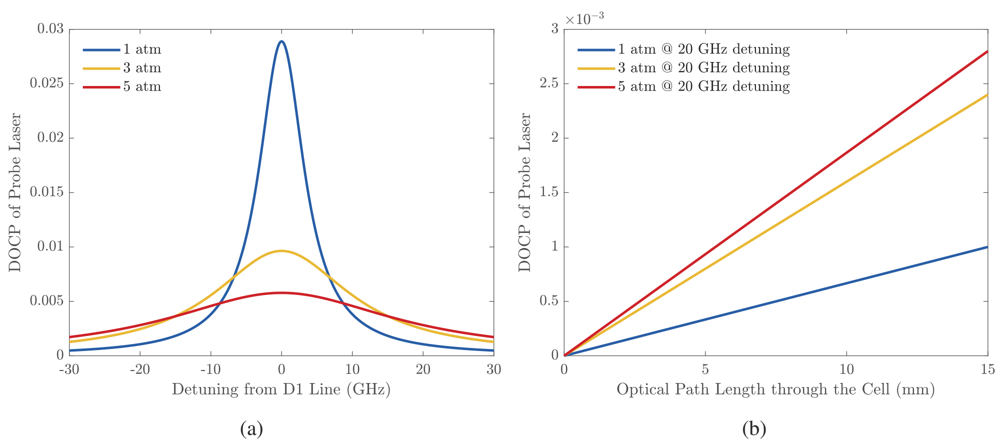

Fig. 2. The DOCP introduced by circular dichroism of atomic spin ensembles.

In addition to the above-mentioned circular dichroism, the spherical co-magnetometer cell wall can also introduce the elliptical polarization of the probe beam due to the stress-induced birefringence effect and the high temperature-induced thermal expansion effect [2]. Since the thermal expansion effect only slightly affects the optical path at the cell wall where the probe beam crosses , the birefringence effect is mainly considered in this section.

Considering the pressure difference between the inside and outside of the cell wall as the principal stress σ_p, a stress-optic analysis is performed on the micro wall volume at the incident point, as shown in Fig. 3. Define the normal vector of the surface of the micro wall volume as $\vec{n}$, and the probe beam with power I enters the wall at an angle β with $\vec{n}$ ($\beta = 0$ when normal incidence), then the effective laser power component affected by stress-induced birefringence

Optics EXPRESS

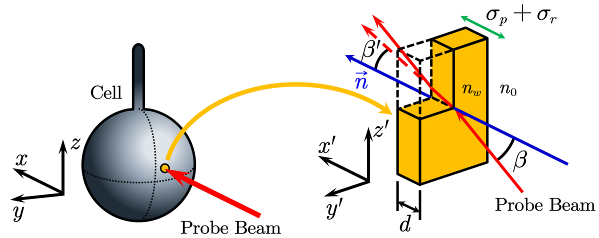

Fig. 3. The schematic diagram of the stress-optic analysis at the incident point.

[38–40] is $I_e = I\sin^2\beta$. The refractive indices of wall and air are n_w and n_0, respectively, which can derive the refraction angle β'. The residual stress contained in the cell wall material is σ_r.

Then according to the Wertheim law [41–43] and neglecting the Poisson's effect, the stress-induced optical retardation can be deduced as follows.

$$\delta_\sigma = \alpha(\sigma_p + \sigma_r)d\tan\beta' \tag{19}$$

where α is the stress optical coefficient and d is the cell wall thickness. Hence the DOCP s_w can be expressed further in the case that δ_σ and $\beta \approx 0$.

$$s_w = sin\delta_\sigma \sin^2\beta = \alpha(\sigma_p + \sigma_r)d\beta'\beta^2 = \alpha(\sigma_p + \sigma_r)\beta^2\frac{d}{n_0} \tag{20}$$

It is noted that, from Eq. (20), the DOCP caused by the spherical cell wall can be considered as a constant and is dominated by the pressure in the cell and the collimation of the optical path.

In summary, considering the terms of DOCPs respectively introduced by the probe laser, circular dichroism of the atomic spin ensembles, and stress-induced birefringence effect of the cell wall simultaneously, all three DOCPs will contribute to the transverse light-shift with equal weight, thus the total one L_x^{tot} experienced by the electrons can be modeled as below.

$$\begin{aligned} L_x^{tot} &= L_x^{laser} + L_x^{atom} + L_x^{wall} \\ &= \frac{\Phi r_e cf}{A\gamma_e}\frac{\nu-\nu_0}{(\nu-\nu_0)^2+(\Gamma/2)^2}\cdot s_l + \int_0^{\mathcal{L}}\frac{\Phi r_e cf}{A\gamma_e}\frac{\nu-\nu_0}{(\nu-\nu_0)^2+(\Gamma/2)^2}\cdot s_a(l)\mathrm{d}l \\ &\quad + \frac{\Phi r_e cf}{A\gamma_e}\frac{\nu-\nu_0}{(\nu-\nu_0)^2+(\Gamma/2)^2}\cdot s_w \\ &= \frac{\Phi r_e cf}{A\gamma_e}\frac{\nu-\nu_0}{(\nu-\nu_0)^2+(\Gamma/2)^2}\cdot\left[s_l + s_w + \int_0^{\mathcal{L}} s_a(l)\mathrm{d}l\right] \\ &= \frac{\Phi r_e cf}{A\gamma_e}\frac{\nu-\nu_0}{(\nu-\nu_0)^2+(\Gamma/2)^2}\cdot\left[s_l + \alpha(\sigma_p+\sigma_r)\beta^2\frac{d}{n_0} + \int_0^{\mathcal{L}}\frac{2\delta(l)}{1+\delta^2(l)}\mathrm{d}l\right] \end{aligned} \tag{21}$$

According to Eq. (21), when maintaining a constant probe laser frequency and power, the transverse light-shift induced by the entire cell $L_x^{cell} = L_x^{atom} + L_x^{wall}$ is constant and has nothing to do with the DOCP s_l of the incident laser. Therefore, the proportion of L_x^{laser} introduced by the probe laser in the total one L_x^{tot} can be effectively changed by modulating the DOCP s_l of the incident laser. As shown in Fig. 4, the transverse light-shifts L_x^{laser} and L_x^{cell} are mixed together to be experienced by electrons such that any measurement method can only reflect the total L_x^{tot}, in the process of DOCP regulation, one can reach two meaningful values of DOCP, which are respectively denoted as the "decoupling point" and "suppression point" of the total transverse light-shift:

1. when at the decoupling point, i.e., $s_l = 0$, the transverse light-shift introduced by probe laser is suppressed, but the total one $L_x^{tot} \neq 0$, which is consistent with the experimental results stated in Section 5. In this case, one can decouple and measure the value of L_x^{cell} component introduced by the entire co-magnetometer cell.

2. when at the suppression point, i.e., $s_l = -s_w - \int_0^{\mathcal{L}} s_a(l)\mathrm{d}l$, the transverse light-shift introduced by the probe laser cancels the entire cell-induced one out and the zeroing of the total term $L_x^{tot} = 0$ can be achieved.

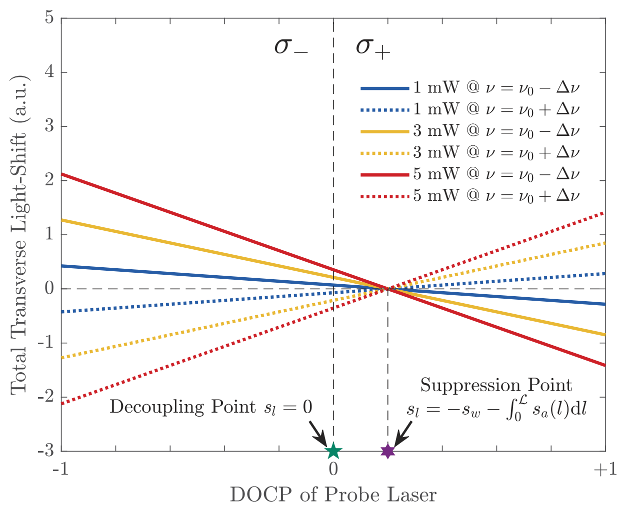

Fig. 4. The theoretical results of variation curves of total transverse light-shift with DOCP at different probe laser powers. The colored solid and dashed lines represent the cases of probe laser frequency of $\nu = \nu_0 \pm \Delta\nu$, respectively, where ν_0 denotes the D1 transition of Rubidium 87 (about 377.1075 THz) and the applied detuning is $\Delta\nu = 50$ GHz.

3. Experimental setup

In order to verify the validity and theoretical conclusions of the measurement, decoupling and suppression methods proposed in Section 2, we perform experiments in a compact SERF co-magnetometer as shown in Fig. 5. The structure of the apparatus is similar to those in our previous work [36,44], and the difference lies in the insertion of a rotatable quarter-wave plate (QWP) in front of the cell in the probe optical path in order to realize the DOCP regulation scheme. The 8 mm diameter spherical cell contains about 1.77 amagat of ^{21}Ne, 50 Torr of nitrogen quenching gas and a mixture of potassium and rubidium. The density ratio between potassium and rubidium is about 1:180 obtained by the alkali metal absorption spectroscopy [45]. The co-magnetometer cell is heated to 458 K within the oven made of boron nitride, and the three-axis magnetic field coils can compensate the magnetic field inner the triple magnetic shields to an expected compensation point. Through the pump optical path, a distributed Bragg reflector (DBR) laser device generates the pump laser with a center frequency of the D1 transition of Potassium (about 389.2862 THz), which is locked by saturated absorption technology [46,47]. PBS7 and QWP are applied to produce a left-handed circularly polarized laser. A pair of planoconvex lenses PL1 and PL2 can expand the spot diameter to 8 mm to ensure that the pump beam can cover the entire cell. The remaining parts form the laser power stabilization system [34,48]. Then for the probe optical path, besides the same laser power stabilization system as above, the balanced polarimeter can realize the high-sensitivity measurement of the optical

Optics EXPRESS

rotation angle. A QWP is mounted on the high-precision rotation mount with the part number PRM05, from Thorlabs to achieve the angle adjustment with the resolution of 10 arcmin.

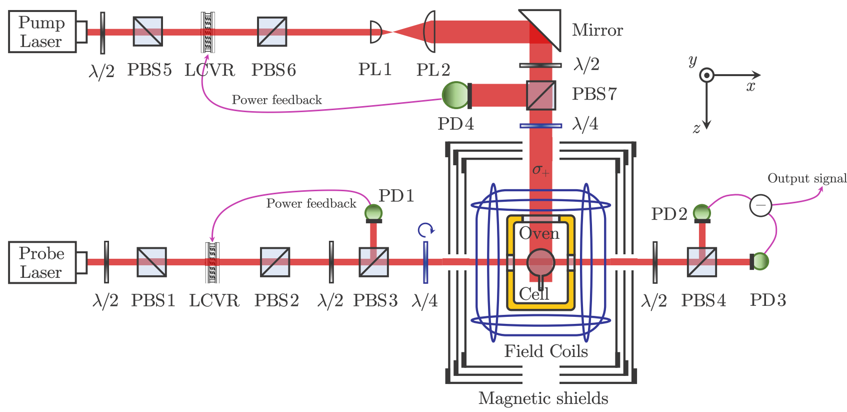

Fig. 5. Schematic diagram of the SERF co-magnetometer. PBS, polarization beam splitter; LCVR, liquid crystal variable retarder; PD, photodiode; PL, planoconvex lenses.

4. Measurement method and experimental verification

According to the theoretical analysis of the measurement method in Section 2, the first step is to carry out the calibration of a series of coefficients C_k. One can adjust the feedback voltage setting of photodiode PD1 to reach the switching between different incident probe laser power, for which 10 different laser power points to be tested are determined and listed in Table 1.

Table 1. Measurement data of the total transverse light-shift L_x^{tot} at different probe laser power points.

No. k	1	2	3	4	5
I_k (mW)	10.44	9.29	8.14	6.99	5.84
C_k (mV/nT)	-36.05	-35.47	-35.26	-33.74	-32.97
ΔS_k (mV)	0.272	-0.655	-1.005	-1.878	-2.307
L_{xk}^{tot} (pT)	-198.60	-172.58	-162.56	-135.40	-121.09
No. k	6	7	8	9	10
I_k (mW)	4.69	4.12	3.54	2.97	2.39
C_k (mV/nT)	-28.36	-27.27	-26.01	-23.53	-19.82
ΔS_k (mV)	-2.906	-2.985	-3.119	-3.211	-2.996
L_{xk}^{tot} (pT)	-88.58	-81.60	-71.14	-54.61	-39.88

The calibration results C_k can be obtained by determining the slope of the curve that ESSR versus the ambient field B_x, and Fig. 6(a) depicts the calibration process under the probe laser power of 3.54 mW. Theoretically, Eq. (10) indicates that the magnitude of calibration results $|C_k|$ should be proportional to the probe laser power I_k, whereas in practice, the probe-induced pumping effect is amplified as the power increases, which shapes the profile closer to be quadratic as Fig. 6(b) shown. This quasi-quadratic correlation can also be manifested in the profile of scale factor versus probe laser power of the co-magnetometer.

Then, we choose the maximum laser power to be tested of $I_1 = 10.44$ mW as the starting point of L_x measurement and implement the compensation field on the transverse and longitudinal directions based on it. After that, an asymmetric modulation with peak-peak amplitude of

Optics EXPRESS

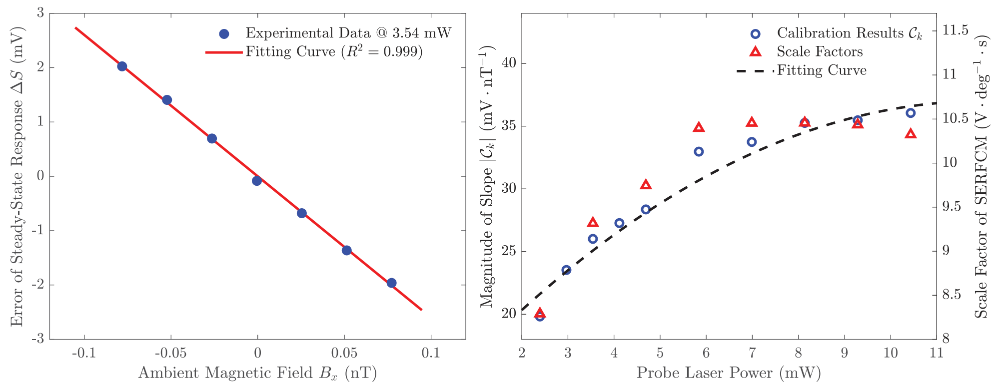

(a) (b)

Fig. 6. The calibration process and results of coefficients C_k ($k = 1, 2, \ldots, 10$): (a) ESSR ΔS varies with the ambient magnetic field B_x at the probe laser power point $I = 3.54$ mW, and C_k can be obtained by fitting the slope of B_x-ΔS curve. (b) The magnitudes of experiment results of calibration coefficients $|C_k|$ and scale factors both perform a nonlinear correlation with respect to the probe laser power.

$\Delta B_z = 0.8$ nT is employed to generate an ESSR signal. In that case, one can switch the probe laser power from I_1 to I_N in sequence and record the corresponding ESSR data. According to the measurement method proposed in Section 2, whose nature is to achieve the measurement of the relative variation of L_x between different laser power points, the relevant measurement results are shown in Fig. 7(a): The hollow circle and dashed line respectively represent the measurement results of the relative variation of transverse light-shift δL_x and corresponding fitting line, where $\delta L_{x1} = 0$ since I_1 is the start point. Ultimately, the I-δL_x line can be translated to cross the origin to obtain the estimated results of total transverse light-shift, which is listed in Table 1, and the measurement error of L_x is related to the fitting precision of the intercept of the I-δL_x line, generally speaking, the error bars increase with the slope of the I-δL_x line, i.e., the DOCP of probe laser $\partial L_x / \partial \Phi = s_l$. Afterwards, we have repeated the experiment 3 times in order to verify the results, and the mean values of repeated measurement results are as shown in Fig. 7(b).

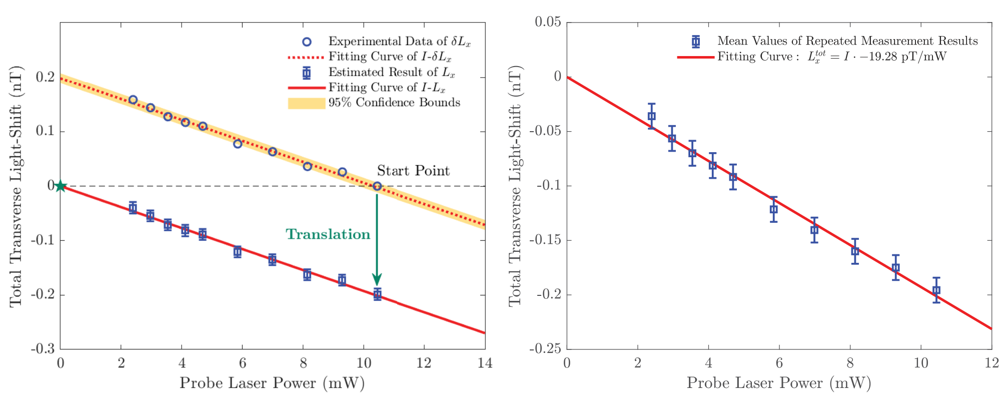

(a) (b)

Fig. 7. The measurement results of the total transverse light-shift. (a) The I-δL_x line can be translated to cross the origin to obtain the estimated results of total transverse light-shift. (b) The mean values of 3 times repeated measurement results.

Optics EXPRESS

5. Decoupling and suppression methods and experimental verification

The theory presented in Section 2 indicates that there are three sources of the transverse light-shift of SERF co-magnetometer: the probe laser, the circular dichroism of the atomic spin ensembles, and the stress-induced birefringence effect of the cell wall. Therefore, a single minimization of the magnitude of DOCP of the probe beam to approximate $s_l = 0$ may not achieve the complete elimination of L_x^{tot}. To validate this point of view, a QWP is inserted into the optical path between PBS3 and cell, and a high-precision rotation mount is implemented to achieve the angle adjustment with the resolution of 10 arcmin such that one can finely regulate the DOCP s_l of the incident probe laser.

Before we integrate these elements above on the compact SERF co-magnetometer, the fast axis of the QWP is roughly aligned with the 0° scale of the mount, and the 0° direction of the fast axis is defined as the z-axis direction, thus the scale value of the mount θ_M can coarsely represent the fast axis angle θ_{FA} of the QWP. Then the DOCP regulation function was examined offline by the rotating quarter-wave plate method [49], the relation between θ_M and DOCP s_l of incident laser in a narrow range around $\theta_M = 90°$ is calibrated, and the results are shown in Fig. 8. Theoretically, the DOCP s_l of the probe laser is perfectly sinusoidal with respect to the fast axis angle θ_{FA} of the QWP, and the derivative of the theoretical curve (black line) at $\theta_{FA} = 90°$ is $\pi/90$, which is agree with the slope of the fitting curve (red dash line) of the experimental data. According to that, DOCP s_l can be considered to vary linearly in the range of $\theta_M = 90° \pm 4°$. Due to device performance and mounting errors, etc., the actual test results indicate a deviation of about 0.5° between θ_M and θ_{FA}, thus the zero crossing point (green pentagram) implies that $\theta_M = 90°33'$ is the actual decoupling point.

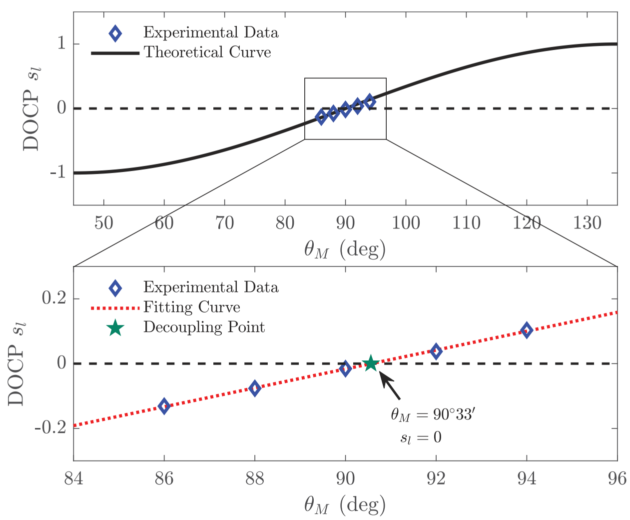

Fig. 8. The offline measurement for the DOCP of the probe laser by the rotating quarter-wave plate method, where the DOCP can be regulated by a QWP with rotation mount.

The rotation angle of the mount of QWP, i.e., θ_M, is regulated to adjust the DOCP s_l of the probe laser, based on which the total transverse light-shift L_x^{tot} is measured under different laser power. In order to make the results more intuitive, the logarithmic axes are employed to plot them as Fig. 9(a) depicted, which demonstrates that the magnitude of transverse light-shift grows with the probe laser power, and the direction of the variation is related to the positive or negative sign of the introduced DOCP s_l. Then the relation between θ_M and L_x^{tot} is as shown in Fig. 9(b), which agrees with the theoretical profiles plotted in Fig. 4, Section 2. It is noteworthy that a certain experimental point $\theta_M = 90°50'$ (purple hexagram) is very close to the theoretical location of the suppression point, and the location of decoupling point is obtained from the zero crossing point in Fig. 8, i.e., $\theta_M = 90°33'$ (green pentagram). In addition, the error bars of the measurement results are improved with the decreasing of the magnitude of DOCP due to the fitting precision.

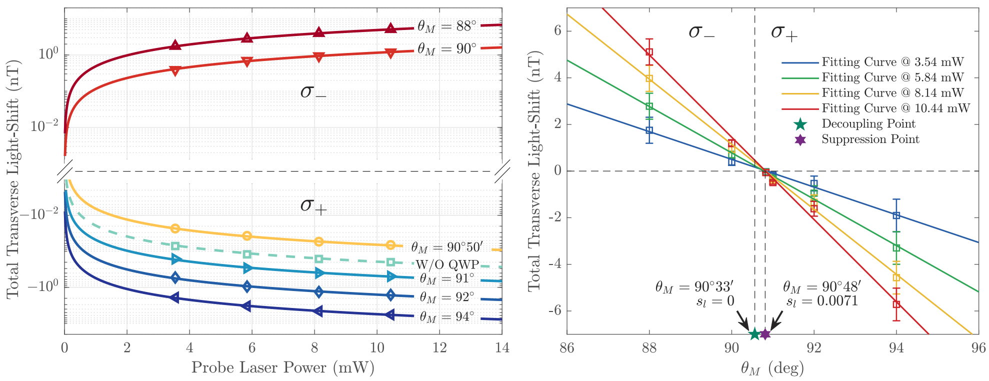

(a) (b)

Fig. 9. The measurement results of the total transverse light-shift under different conditions: (a) The relation between L_x^{tot} and probe laser power under different DOCP s_l, the DOCP s_l is regulated by θ_M. The measurement result of the green dash line is obtained from Section 4 and there is absence of QWP. (b) The relation between L_x^{tot} and θ_M under different probe laser power, where the decoupling point is obtained from the fitted zero crossing point in Fig. 8 and $\theta_M = 90°50'$ is very close to the theoretical location of the suppression point.

According to Fig. 9(a), by regulating the DOCP of the probe laser into the suppression point, the transverse light-shift is clearly reduced and related data is recorded in Table 2. Then from Fig. 9(b), one can directly read out the decoupling measurement results of the transverse light-shift introduced by the whole cell of the compact SERF co-magnetometer at each laser power point under the fitted decoupling point $\theta_M = 90°33'$, which satisfies the expression $L_x^{cell} = I \cdot -43.86$ pT/mW.

Table 2. Measurement data of the total transverse light-shift L_x^{tot} at decoupling point and suppression point.

Probe laser power (mW)	3.54	5.84	8.14	10.44
L_x^{cell} @ decoupling point (pT)	169.2	224.3	368.8	461.6
L_x^{tot} @ suppression point (pT)	-23.2	-37.0	-53.8	-66.4
L_x^{tot} W/O QWP (pT)	-71.1	-121.0	-162.6	-198.6
Suppression ratio	67%	69%	67%	67%

By this DOCP regulation scheme, the sensitivity of the transverse light-shift to the probe laser power fluctuations is also significantly suppressed, which can be examined by the measurement of ESSR and as shown in Fig. 10. The variation of the transverse magnetic field caused by the fluctuation of probe laser power can significantly result in the ESSR, while this magnetic-optic coupling effect is well suppressed by the canceling of L_x^{tot} at the suppression point. Furthermore, the specific theoretic expression of the quadratic curves in Fig. 10 is mentioned as Eq. (8).

Furthermore, DOCP can also affect the long-term stability and sensitivity performance of SERF co-magnetometer, as depicted in Fig. 11. The total transverse light-shift L_x^{tot} increases apparently as the improvement of DOCP s_l, which leads the transverse field to deviate from zero and reduces the sensitivity of SERF co-magnetometer, as confirmed by the experiment results in Fig. 11(b) and 11(d). In order to consider both the efficiency of the experiment and

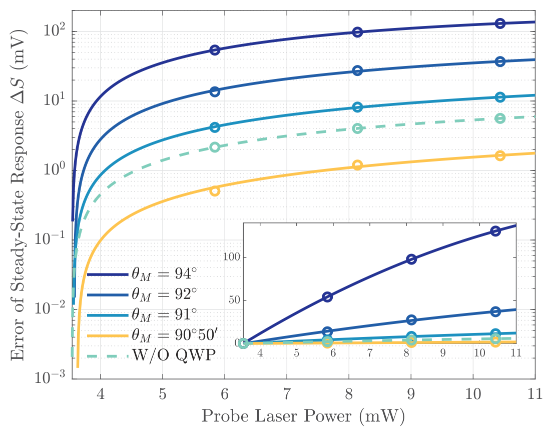

Fig. 10. The quadratic variation curves of ESSR with probe laser power under different DOCP s_l. The inset shows the quadratic profiles of ESSR on the linear axes.

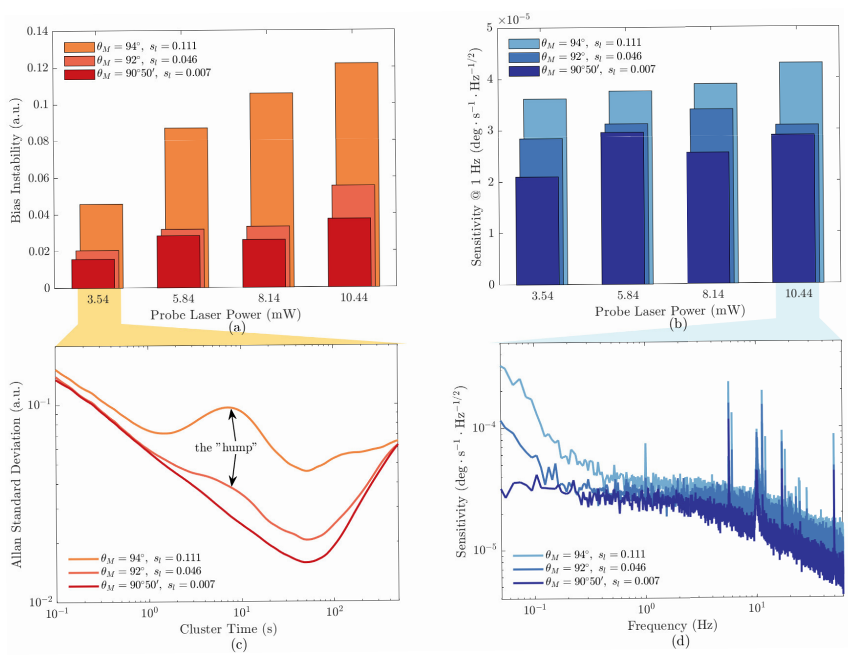

Fig. 11. The long-term stability and sensitivity performance of SERF co-magnetometer under different DOCP s_l and different probe laser power. (a) The bias stability of SERF co-magnetometer output signal under different conditions, which can be represented by the flat line's corresponding Allan standard deviation value [51]. (b) The sensitivity values of SERF co-magnetometer output signal at a frequency of 1 Hz under different conditions. (c) The Allan standard deviation curves with a certain probe laser power I = 3.54 mW under different DOCP s_l. (d) The sensitivity curves with a certain probe laser power I = 10.44 mW under different DOCP s_l.

the accurate assessment of long-term stability, the output signal of SERF co-magnetometer is collected for 2 hours under different conditions, according to which the Allan deviation can be obtained to present the bias instability of SERF co-magnetometer. As shown in Fig. 11(a) and 11(c), when under the same probe laser power, the increasing of DOCP s_l can explicitly result in a "hump" at the cluster time of about 10 s,which is consistent with some properties of exponentially correlated (Markov) noise [50], such that the bias instability gets worse. And at the cluster time of 500 s and beyond, Allan variance is dominated by the manifested rate ramp, which is mainly correlated to the slow change in temperature (including the cell temperature and ambient temperature) instead of the magnetic-optic coupling effect induced by the transverse light-shift. Therefore, by regulating the DOCP of probe laser to the suppression point under any probe laser power, the long-term stability and sensitivity performance of SERF co-magnetometer can both be effectively improved.

6. Conclusion

In conclusion, in this paper, we firstly proposed a novel measurement method for fast measurement of the transverse light-shift based on the ESSR of co-magnetometers, whose error depends only on DOCP of the probe laser. Then we model and analyze the sources of transverse light-shift in a compact SERF co-magnetometer from three aspects: the non-ideal linear polarization of probe laser, the circular dichroism of the atomic spin ensembles, and the stress-induced birefringence effect of the cell wall. According to the theory model, we further suggest the decoupling and suppression methods of transverse light-shift based on a DOCP regulation scheme. When at the decoupling point, the transverse light-shift is induced by the whole co-magnetometer cell only, such that we can obtain the decoupling measurement results $L_x^{cell} = I \cdot -43.86$ pT/mW, and at the suppression point, the transverse light-shift introduced by the probe laser and the whole cell cancel each other out, such that the total transverse light-shift can be zeroing theoretically. The experimental results demonstrate that our method achieves the total transverse light-shift suppression of more than 67%, and the short- and long-term performance of SERF co-magnetometer are improved due to the reduction of the coupling effect between the probe laser power and transverse field. In practical engineering, further reduction of transverse light-shift can be realized by employing a cubic cell wall instead of the spherical one, and the properly adjustment of the pressure in the cell and the probe laser frequency. Moreover, the measurement, decoupling and suppression methods provided in this paper also have the potential to be applied to other atomic sensors, such as the SERF magnetometers and nuclear spin co-magnetometers.

Funding. Special Project for Research and Development in Key areas of Guangdong Province (2021B0101410005); National Natural Science Foundation of China (62103026, 61673041).

Disclosures. The authors declare that there are no conflicts of interest related to this article.

Data availability. Data underlying the results presented in this paper are not publicly available at this time but may be obtained from the authors upon reasonable request.

References

1. T. W. Kornack and M. V. Romalis, “Dynamics of two overlapping spin ensembles interacting by spin exchange,” Phys. Rev. Lett. **89**(25), 253002 (2002).
2. T. W. Kornack, “A test of cpt and lorentz symmetry using a potassium-helium-3 co-magnetometer,” Ph.D. thesis, Princeton University. (2005).
3. J. M. Brown, “A new limit on lorentz- and cpt-violating neutron spin interactions using a potassium-helium comagnetometer,” Ph.D. thesis, Princeton University. (2011).
4. T. W. Kornack, R. K. Ghosh, and M. V. Romalis, “Nuclear spin gyroscope based on an atomic co-magnetometer,” Phys. Rev. Lett. **95**(23), 230801 (2005).
5. R. Li, W. Fan, L. Jiang, L. Duan, W. Quan, and J. Fang, “Rotation sensing using a K-Rb-21Ne comagnetometer,” Phys. Rev. A **94**(3), 032109 (2016).
6. C. Qingzhong, Y. Gongliu, Q. Wei, S. Ningfang, T. Yongqiang, and L. Yiliang, “Error analysis of the K-Rb-21Ne comagnetometer space-stable inertial navigation system,” Sensors **18**(3), 670 (2018).

7. J. Fang and J. Qin, "Advances in atomic gyroscopes: A view from inertial navigation applications," Sensors **12**(5), 6331–6346 (2012).
8. F. Allmendinger, W. Heil, S. Karpuk, W. Kilian, A. Scharth, U. Schmidt, A. Schnabel, Y. Sobolev, and K. Tullney, "New limit on lorentz-invariance-and c p t-violating neutron spin interactions using a free-spin-precession He 3-Xe 129 comagnetometer," Phys. Rev. Lett. **112**(11), 110801 (2014).
9. V. Flambaum and M. V. Romalis, "Limits on lorentz invariance violation from coulomb interactions in nuclei and atoms," Phys. Rev. Lett. **118**(14), 142501 (2017).
10. M. Smiciklas, J. M. Brown, L. W. Cheuk, S. J. Smullin, and M. V. Romalis, "New test of local lorentz invariance using a 21Ne-Rb-K comagnetometer," Phys. Rev. Lett. **107**(17), 171604 (2011).
11. L. Hunter, J. Gordon, S. Peck, D. Ang, and J.-F. Lin, "Using the earth as a polarized electron source to search for long-range spin-spin interactions," Science **339**(6122), 928–932 (2013).
12. G. Vasilakis, J. M. Brown, T. W. Kornack, and M. V. Romalis, "Limits on new long range nuclear spin-dependent forces set with a K-3He co-magnetometer," Phys. Rev. Lett. **103**(26), 261801 (2009).
13. M. Bulatowicz, R. Griffith, M. Larsen, J. Mirijanian, and T. G. Walker, "Laboratory search for a long-range t-odd, p-odd interaction from axionlike particles using dual-species nuclear magnetic resonance with polarized 129xe and 131xe gas," Phys. Rev. Lett. **111**(10), 102001 (2013).
14. M. Jiang, H. Su, A. Garcon, X. Peng, and D. Budker, "Search for axion-like dark matter with spin-based amplifiers," Nat. Phys. **17**(12), 1402–1407 (2021).
15. S. Appelt, B. A. Baranga, C. J. Erickson, M. V. Romalis, and W. Happer, "Theory of spin-exchange optical pumping of 3he and 129xe," Phys. Rev. A **58**(2), 1412–1439 (1998).
16. S. J. Seltzer, *Developments in alkali-metal atomic magnetometry* (Princeton University, 2008).
17. E. Zhivun, A. Wickenbrock, J. Sudyka, S. Pustelny, and D. Budker, "Light shift averaging in paraffin-coated alkali vapor cells," Opt. Express **24**(14), 15383–15390 (2016).
18. J. Allred, R. Lyman, T. Kornack, and M. V. Romalis, "High-sensitivity atomic magnetometer unaffected by spin-exchange relaxation," Phys. Rev. Lett. **89**(13), 130801 (2002).
19. Quan Wei, Wei Kai, and Li Hairong, "Precision measurement of magnetic field based on the transient process in a K-Rb-21Ne co-magnetometer," Opt. Express **25**(8), 8470–8483 (2017).
20. I. A. Sulai, R. Wyllie, M. Kauer, G. S. Smetana, and T. G. Walker, "Diffusive suppression of ac-stark shifts in atomic magnetometers," Opt. Lett. **38**(6), 974–976 (2013).
21. Y. Chen, W. Quan, S. Zou, Y. Lu, L. Duan, Y. Li, H. Zhang, M. Ding, and J. Fang, "Spin exchange broadening of magnetic resonance lines in a high-sensitivity rotating K-Rb-21Ne co-magnetometer," Sci. Rep. **6**, 36547 (2016).
22. R. Li, W. Quan, W. Fan, L. Xing, Z. Wang, Y. Zhai, and J. Fang, "A dual-axis, high-sensitivity atomic magnetometer," Chin. Phys. B **26**(12), 120702 (2017).
23. L. Jiang, Q. Wei, R. Li, L. Duan, and J. Fang, "Suppression of the cross-talk effect in a dual-axis k rb ne 21 comagnetometer," Phys. Rev. A **95**(6), 062103 (2017).
24. Y. Chen, W. Quan, L. Duan, Y. Lu, L. Jiang, and J. Fang, "Spin-exchange collision mixing of the k and rb ac stark shifts," Phys. Rev. A **94**(5), 052705 (2016).
25. Wei Kai, Zhao Tian, Fang Xiujie, Zhai Yueyang, and Quan Hairong, "In-situ measurement of the density ratio of k-rb hybrid vapor cell using spin-exchange collision mixing of the K and Rb light shifts," Opt. Express **27**(11), 16169–16183 (2019).
26. A. V. Semenko, G. S. Belotelov, D. V. Sutyrin, S. N. Slyusarev, and V. G. Pal'Chikov, "Uncertainty analysis of the frequency standard on cold ytterbium atoms using the operational parameters of the optical lattice," Quantum Electron. **51**(6), 484–489 (2021).
27. R. J. Rengelink, D. Van, R. Notermans, R. Jannin, K. Eikema, M. Hoogerland, and W. Vassen, "Precision spectroscopy of helium in a magic wavelength optical dipole trap," Nat. Phys. **14**(11), 1132–1137 (2018).
28. Y. Jia, Z. Liu, M. Ding, Z. Chai, and W. Wu, "The effect of tensor light shift on residual magnetic field compensation in a nuclear spin co-magnetometer," Appl. Phys. Lett. **116**(14), 142405 (2020).
29. L. Xing, W. Quan, T. Song, Q. Cai, and W. Ye, "A measurement method of transverse light-shift in atomic spin co-magnetometer," arXiv e-prints (2021).
30. Y. Fu, W. Fan, J. Ruan, Y. Liu, Z. Lu, and W. Quan, "Effects of probe laser intensity on co-magnetometer operated in spin-exchange relaxation-free regime," IEEE Trans. Instrum. Meas. **71**, 1–7 (2022).
31. M. I. Vaskovskaya, E. A. Tsygankov, D. S. Chuchelov, S. A. Zibrov, and V. L. Velichansky, "Effect of the buffer gases on the light shift suppression possibility," Opt. Express **27**(24), 35856 (2019).
32. G. Vasilakis, *Precision measurements of spin interactions with high density atomic vapors* (Princeton university, 2011).
33. D. Miletic, C. Affolderbach, M. Hasegawa, R. Boudot, C. Gorecki, and G. Mileti, "Ac stark-shift in cpt-based cs miniature atomic clocks," Appl. Phys. B **109**(1), 89–97 (2012).
34. L. Xing, Y. Zhai, W. Fan, J. Huang, T. Song, W. Ye, and W. Quan, "Miniaturized optical rotation detection system based on liquid crystal variable retarder in a k-rb-21 ne gyroscope," Opt. Express **27**(26), 38061–38070 (2019).
35. Yao Han, Danyue Yang, Cai Jiashu, Zhao Junpeng, and Ding Ming, "Acousto-optic modulation detection method in an all-optical k-rb hybrid atomic magnetometer using uniform design method," Opt. Express **26**(22), 28682–28692 (2018).

Optics EXPRESS

36. W. Fan, G. Liu, R. Li, W. Quan, L. Jiang, and L. Duan, "A three-axis atomic magnetometer for temperature-dependence measurements of fields in a magnetically shielded environment," Meas. Sci. Technol. **28**(9), 095007 (2017).
37. Y.-K. Ho, B.-H. Zhang, and Z.-S. Yuan, "Probability and selection rule for nuclear excitation by electron transition," Phys. Rev. C **44**(5), 1910–1914 (1991).
38. Z. Wang, Z. Wu, Y. Han, K. Kang, and C. Li, "Metal stress-optic effect and its application in stress measurement," Thin Solid Films **695**, 137755 (2020).
39. J. G. Suh, J. S. Hawong, and D. C. Shin, "A study of the development of the stress optic law of photoelastic experiment considering residual stress," Ksme Int. J. **17**(11), 1674–1681 (2003).
40. M. K. Szczurowski, T. Martynkien, G. Statkiewicz-Barabach, W. Urbanczyk, L. Khan, and D. J. Webb, "Measurements of stress-optic coefficient in polymer optical fibers," Opt. Lett. **35**(12), 2013–2015 (2010).
41. G. Wertheim, *Mémoire sur la double réfraction temporairement produite dans les corps isotropes: suivi de Note sur la relation entre la composition chimique et entre l'élasticité des minéraux à élasticité constante* (imprimerie Mallet-Bachelier, 1854).
42. L. Ainola and H. Aben, "On the generalized wertheim law in integrated photoelasticity," J. Opt. Soc. Am. A **25**(8), 1843 (2008).
43. A. Kuske and G. Robertson, Photoelastic stress analysis (1974).
44. Z. Wang, S. Liu, R. Wang, L. Yuan, J. Huang, Y. Zhai, and S. Zou, "Atomic spin polarization controllability analysis: A novel controllability determination method for spin-exchange relaxation-free co-magnetometers," IEEE/CAA J. Autom. Sinica **9**(4), 699–708 (2021).
45. W. Quan, K. Shen, Y. Zhai, X. Wang, L. Jiang, W. Fan, F. Liu, J. Qin, and S. Wan, "Precision measurements of optically thick alkali metal number density within a hybrid alkali metal cell," Appl. Opt. **57**(20), 5714–5719 (2018).
46. W. Demtröder, *Laser spectroscopy: basic concepts and instrumentation* (Springer Science & Business Media, 2013).
47. S. A. Knappe, H. G. Robinson, and L. Hollberg, "Microfabricated saturated absorption laser spectrometer," Opt. Express **15**(10), 6293–6299 (2007).
48. J. Huang, Z. Wang, W. Fan, L. Xing, W. Zhang, L. Duan, and W. Quan, "Analysis and suppression of the polarization error for the optical rotation detection system in an atomic comagnetometer," Opt. Express **28**(24), 35748–35760 (2020).
49. B. Schaefer, E. Collett, R. Smyth, D. Barrett, and B. Fraher, "Measuring the stokes polarization parameters," Am. J. Phys. **75**(2), 163–168 (2007).
50. Ieee standard specification format guide and test procedure for single-axis laser gyros, in IEEE Std 647-2006 (Revision of IEEE Std 647-1995), (2006).
51. Jiang Liwei, Quan Wei, Liang Yixiang, Liu Jiali, and Duan Lihong, "Effects of pump laser power density on the hybrid optically pumped comagnetometer for rotation sensing," Opt. Express **27**(20), 27420–27430 (2019).